The Role of Oceans and Sea Ice in Abrupt Transitions between Multiple Climate States

BRIAN E. J. ROSE

Department of Atmospheric Sciences, University of Washington, Seattle, Washington

DAVID FERREIRA AND JOHN MARSHALL

Department of Earth, Atmospheric and Planetary Sciences, Massachusetts Institute of Technology, Cambridge, Massachusetts

ABSTRACT

The coupled climate dynamics underlying large, rapid, and potentially irreversible changes in ice cover are studied. A global atmosphere–ocean–sea ice general circulation model with idealized aquaplanet geometry is forced by gradual multi-millennial variations in solar luminosity. The model traverses a hysteresis loop between warm ice-free conditions and cold glacial conditions in response to ± 5 W m^{-2} variations in global, annual-mean insolation. Comparison of several model configurations confirms the importance of polar ocean processes in setting the sensitivity and time scales of the transitions. A "sawtooth" character is found with faster warming and slower cooling, reflecting the opposing effects of surface heating and cooling on upper-ocean buoyancy and, thus, effective heat capacity. The transition from a glacial to warm, equable climate occurs in about 200 years.

In contrast to the "freshwater hosing" scenario, transitions are driven by radiative forcing and sea ice feedbacks. The ocean circulation, and notably the meridional overturning circulation (MOC), does not drive the climate change. The MOC (and associated heat transport) collapses poleward of the advancing ice edge, but this is a purely passive response to cooling and ice expansion. The MOC does, however, play a key role in setting the time scales of the transition and contributes to the asymmetry between warming and cooling.

1. Introduction

This study is concerned with the dynamics by which the climate system can undergo large, rapid, and potentially irreversible changes in temperature and ice cover. We impose an external oscillator on a coupled climate model in the form of a slowly varying solar luminosity and (as will be shown) find a nonlinear climatic response with threshold behavior and a variety of faster, internally determined time scales. The experiments are highly idealized but provide a detailed, physically self-consistent look at the coupled atmosphere–ocean–ice processes involved in the growth and retreat of extensive sea ice caps, and an opportunity to diagnose causality in concomitant shifts in ocean circulation and ice cover. They may therefore provide insight into mechanisms for observed large and abrupt climate shifts of the past and guidance in the interpretation of proxy data.

One inspiration for our experiments is millennial-scale climate variability of the last ice age, particularly the sequence of abrupt warming and cooling known as Dansgaard–Oeschger (DO) events. The Greenland ice cores show repeated abrupt warmings $O(15°C)$ (about two-thirds of the full glacial–interglacial difference) occurring in a few decades. Synchronous, though less dramatic, changes have been found throughout the Northern Hemisphere (Seager and Battisti 2007). DO warming is thought to involve large poleward displacements of the North Atlantic sea ice edge (e.g., Gildor and Tziperman 2003; Li et al. 2010). A typical sequence of events has three stages: abrupt warming, several hundred years of slow cooling, and a more rapid cooling back to cold glacial conditions (Rahmstorf 2002).

A central issue in this paper is the interplay among sea ice extent, oceanic stratification, and meridional overturning circulation (MOC). The link between North Atlantic MOC and glacial climate variability was famously drawn by Broecker et al. (1985, 1990). Theories

Corresponding author address: Brian Rose, Department of Atmospheric Sciences, University of Washington, Box 351640, Seattle, WA 98195.
E-mail: brose@atmos.washington.edu

of abrupt climate change, and DO events in particular, have since been dominated by the notion that the MOC plays an active, causal role in cooling and warming. For reviews see Wunsch (2006), Seager and Battisti (2007), and Clement and Peterson (2008).

Broecker (1990) and others suggested that meltwater from continental ice could stabilize the surface North Atlantic sufficiently to suppress deep-water formation and reduce the MOC and associated ocean heat transport (OHT). Manabe and Stouffer (1995) were the first to assess the potential for an MOC shutdown in a so-called "freshwater hosing" model experiment in which a large transient freshwater flux is added to the northern North Atlantic. There is now ample model evidence that such hosing can lead to widespread and long-lived cooling; see, for example, intercomparison studies by Rahmstorf et al. (2005) and Stouffer et al. (2006). The response and recovery time depend on the rate and magnitude of the freshwater perturbation (Stouffer et al. 2006), with some (not all) coupled models apparently showing bistability of the MOC (e.g., Hawkins et al. 2011). Bitz et al. (2007) and Cheng et al. (2007) describe an extreme example in which a large sudden freshening of the North Atlantic produces immediate collapse of the Atlantic MOC and associated North Atlantic Deep Water (NADW) formation and a southward shift in the location of OHT convergence, followed by sea ice expansion and surface cooling. The response is sensitive to the background climate: under Last Glacial Maximum (LGM) conditions sea ice expands over the entire North Atlantic basin poleward of 45°N, while under modern conditions sea ice expansion is mostly confined to the Nordic seas. A surface cooling on the order of 10°C is largely tied to the areas of expanded ice, and thus much more widespread in the LGM case. Cheng et al. argue that the different sensitivities arise from stronger positive sea ice feedbacks in the LGM case, both from surface albedo and interactions with NADW formation.

The hosing paradigm is most naturally associated with *cooling* events in the Northern Hemisphere glacial record (Clement and Peterson 2008). There is observational evidence for coincident changes in NADW formation, MOC, and cooling during Heinrich event H1 (17.5 kyr) and the Younger Dryas (12.7 kyr) (e.g., McManus et al. 2004); it is now widely supposed that "hosing" by glacial meltwater played key roles in those events, despite a number of serious outstanding conceptual problems (Wunsch 2010). The link between hosing experiments and DO events, which feature large and abrupt *warming*, is much more tenuous (Clement and Peterson 2008). There is no compelling evidence that the freshwater balance of the North Atlantic plays a driving role in these events. The hosing scenario, therefore, may be a poor

analog for the most abrupt climate changes of the last glacial. On the other hand, hosing experiments such as Bitz et al. (2007) suggest that the climate system is most sensitive under glacial conditions so that modest perturbations (whether to freshwater budgets or otherwise) might drive substantial variations in sea ice, ocean circulation, and surface temperature. These aspects of the system are irretrievably coupled together in nature and might covary in similar ways in response to different forcings.

Here we explore an alternate paradigm for abrupt climate change, one in which sea ice is the nonlinear player and the ocean sets the time scales of warming and cooling but is not the primary driver. We are emphatically not proposing a new theory for DO events, or any specific paleoclimate problem. Instead, we use idealized coupled general circulation model (GCM) experiments to investigate general mechanisms of large-amplitude climate change. Our simulations are externally driven by slow, imposed solar variations and involve transitions between multiple stable equilibria. Unlike the hosing scenario, the simulated ocean circulation changes are a consequence of, rather than a driver of, the warming/cooling. However, as we will show, these changes have much in common with the hosing scenario: cooling and sea ice expansion are accompanied by a shutting off of high-latitude deep-water formation and equatorward shift of the region of OHT convergence.

We carry out our calculations on an aquaplanet, an earthlike planet with near-total absence of land surfaces. The aquaplanet context has been used in a series of recent papers to investigate the fundamental role of the ocean in setting the mean state of the climate and its variability (Marshall et al. 2007; Enderton and Marshall 2009; Ferreira et al. 2010, 2011). These models strip away complexity in the boundary conditions (distribution of continents, mountains, and ocean bathymetry) while preserving the complexity inherent in the physics of atmosphere–ocean circulation. Geometrical constraints on ocean circulation are reduced to a minimal description with narrow sticklike continents. Ice cover on the aquaplanet is strictly in the form of sea ice and overlying snow. Clearly, insight into real glacial climates from a model without continental ice sheets can only be indirect at best. However, the absence of ice sheets presents a considerable computational advantage since the model can be integrated through complete "glaciation" and "deglaciation"[1] in a few weeks of computer

---

[1] We use these terms for growth/retreat of polar sea ice caps in the aquaplanet.
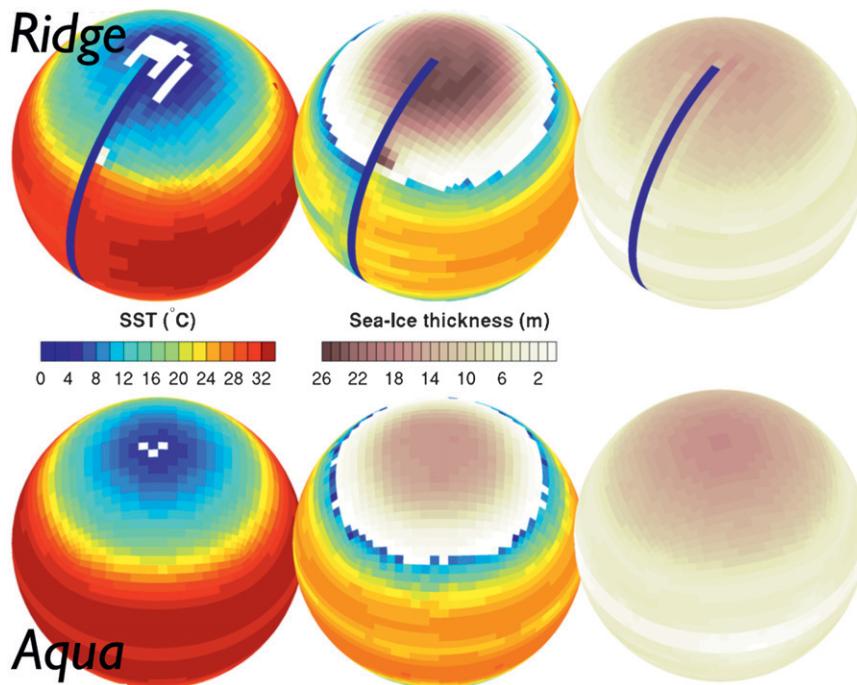
FIG. 1. Multiple equilibria in a coupled atmosphere–ocean–ice GCM in two different idealized
continental configurations, as reported in FMR11.

time without invoking ad hoc parameterizations for at-
mospheric heat, moisture, and momentum fluxes.

Marshall et al. (2007) described coupled simulations
of a pure aquaplanet (zonally unblocked ocean) with
large sea ice caps, focusing on annular mode variability.
Enderton and Marshall (2009) compared a sequence
of different ocean basin geometries to understand the
atmosphere–ocean partition of heat transport and its
relation to sea ice extent. Ferreira et al. (2010) examined
how basin asymmetries set the location of deep-water
formation. Ferreira et al. (2011, hereafter FMR11) re-
cently found multiple equilibria in the same aquaplanet
GCM. Simulations were forced by present-day insola-
tion and greenhouse gas levels and integrated to equi-
librium from different initial conditions, yielding three
vastly different climates: a warm equable climate with-
out polar ice, a much colder climate with midlatitude
sea ice edge, and a completely ice-covered "Snowball"
state. All three states were found in both *Aqua* and
Ridge configurations: the former is a pure aquaplanet
with a flat-bottomed, zonally unblocked, ocean and the
latter has a thin pole-to-pole continent bounding the
ocean into a global-scale basin. The multiple states are
illustrated here in Fig. 1. These results are of potentially
great interest to the study of paleoclimate. Without in-
voking exotic changes in forcing, the aquaplanet model
supports climatic states reminiscent of, for example,

the Eocene, the LGM, and the late Neoproterozoic. It
is thus an efficient numerical laboratory for studying
coupled atmosphere–ocean–ice dynamics involved in
transitions between these vastly different past climates.
The present work focuses on these transient dynamics,
as opposed to the equilibrium issues studied in the
above cited works.

The coexistence of a Snowball state with a modernlike
climate is unsurprising, as this is the robust prediction of
simple albedo feedback models (e.g., Budyko 1969;
North 1990), and has been confirmed in a state-of-the-
art coupled GCM (Marotzke and Botzet 2007). The
novel result in FMR11 is the coexistence of the "Warm"
and "Cold" states (following FMR11, "Cold" refers to
the state with a midlatitude sea ice edge). This has no
analog in traditional energy balance models (EBMs),
despite the key importance of albedo feedback. OHT
plays a key role in stabilizing FMR11's Cold state by
converging heat into the midlatitudes just equatorward
of the ice edge (primarily by wind-driven subtropical
overturning); perturbation studies show that any change
in OHT results in displacement of the ice edge. FMR11
conclude that the meridional structure of OHT (in par-
ticular the tendency of the oceans to warm the mid-
latitudes) is a key ingredient in the maintenance of
multiple states. This result was anticipated by Rose and
Marshall (2009), who extended the diffusive EBM to

include the effects of OHT with meridional structure dictated by surface wind stress.

Ocean heat transport varies both in magnitude and spatial structure between Warm and Cold aquaplanet states (FMR11); changes are of opposite sign in low and high latitudes. More heat is carried out of the tropics in the Cold state, but practically all of it is released to the atmosphere equatorward of the sea ice margin. Particularly in *Ridge*, a deep MOC carries some heat into the high latitudes in the Warm state, and this circulation is absent in the Cold state. Here we address the causality of this change. Is cooling and sea ice expansion driven by a shutdown in MOC akin to the hosing scenario, or does MOC collapse as a consequence of the cooling? Is there any hope of distinguishing such signals in paleo records? We are also interested in asymmetries between warming and cooling, the role of sea ice and the oceans therein, and what, if anything, they might tell us about DO events, glacial/interglacial cycles, or other large-amplitude climate changes on earth.

Our paper is laid out as follows: The model and imposed forcing are described in section 2. In section 3 we compare the shapes of the hysteresis loops generated in three different model configurations (*Aqua*, *Ridge*, and a simple slab ocean). In section 4 we describe a representative glaciation/deglaciation in *Ridge* in detail, paying special attention to the link between OHT and sea ice. Discussion and conclusions follow in sections 5 and 6, respectively.

2. Experimental setup

We perform long integrations of the coupled Massachusetts Institute of Technology GCM (MITgcm) (Marshall et al. 1997, 2004) in "aquaplanet" configuration. Atmosphere, ocean, and sea ice components use the same cubed-sphere grid at coarse C24 resolution (3.75° at the equator), ensuring as much fidelity in model dynamics at the poles as elsewhere. The ocean component is a primitive equation non-eddy-resolving model, using the rescaled height coordinate z^* (Adcroft and Campin 2004) with 15 levels and a flat bottom at 3-km depth (chosen to approximate present-day ocean volume and, thus, total heat capacity). Subgrid-scale parameterizations include advective mesoscale eddy transport (Gent and McWilliams 1990), isopycnal diffusion (Redi 1982), and vertical convective adjustment (Klinger et al. 1996). Vertical diffusivity is uniform at 3×10^{-5} m^2 s^{-1}, and we use a nonlinear equation of state (Jackett and Mcdougall 1995).

The atmosphere is a five-level primitive equation model with moist physics based on the Simplified Parametrizations, Primitive-Equation Dynamics (SPEEDY)

model (Molteni 2003). These include four-band long- and shortwave radiation schemes with interactive water vapor channels, diagnostic clouds, a boundary layer scheme, and mass-flux scheme for moist convection. Pressure coordinates are used in the vertical with one level in the boundary layer, three in the free troposphere, and one in the stratosphere. Details about these parameterizations [substantially cruder than those used in Intergovernmental Panel on Climate Change (IPCC)-class models] are given in Rose and Ferreira (2013). Present-day atmospheric CO_2 is prescribed. Insolation varies seasonally with 23.5° obliquity and zero eccentricity, but there is no diurnal cycle.

The sea ice component is a three-layer thermodynamic model based on Winton (2000) (two layers of ice plus surface snow cover). Prognostic variables include ice fraction, snow and ice thickness, and ice enthalpy accounting for brine pockets with an energy-conserving formulation. Ice surface albedo depends on temperature, snow depth, and age (FMR11). A diffusion of ice thickness is used as a proxy for ice dynamics, representing the net large-scale export of ice from the polar regions. The model achieves machine-level conservation of heat, water, and salt, enabling long integrations without numerical drift (Campin et al. 2008).

Three different ocean configurations are used: *Slab*, *Aqua* and *Ridge*. The *Slab* is a simple 30-m mixed layer aquaplanet with prescribed heat transport (q flux). The q flux was diagnosed from the Cold reference state of *Aqua* and represents both lateral OHT convergence into the mixed layer and seasonal vertical mixing.[2] *Ridge* and *Aqua* (Fig. 1) use full dynamical ocean models (with and without a pole-to-pole barrier) and are identical to the setups in FMR11. The three configurations give a hierarchy of complexity *Slab* < *Aqua* < *Ridge*, particularly in the high-latitude ocean circulation. *Ridge* exhibits the most complex climate changes due to basin dynamics (a subpolar gyre) and high-latitude deep-water formation processes that are absent from *Aqua*. Atmosphere and sea ice formulations are identical in all cases.

We now describe simulations forced by time-varying solar constant S_0 [global, annual-mean incoming solar radiation at the top of atmosphere (TOA)]. All runs are initialized in equilibrium (Warm or Cold) by branching from the FMR11 reference states. We impose sinusoidal S_0 variations $O(5$ W m$^{-2})$ about its reference value (slightly smaller in *Ridge* than in *Aqua*, as discussed in

---

[2] FMR11 showed that *Slab* supports multiple equilibria (Warm and Cold) under certain (but not all) q-flux patterns. Multiple states are not found when OHT is weak or has a broad equator-to-pole scale.
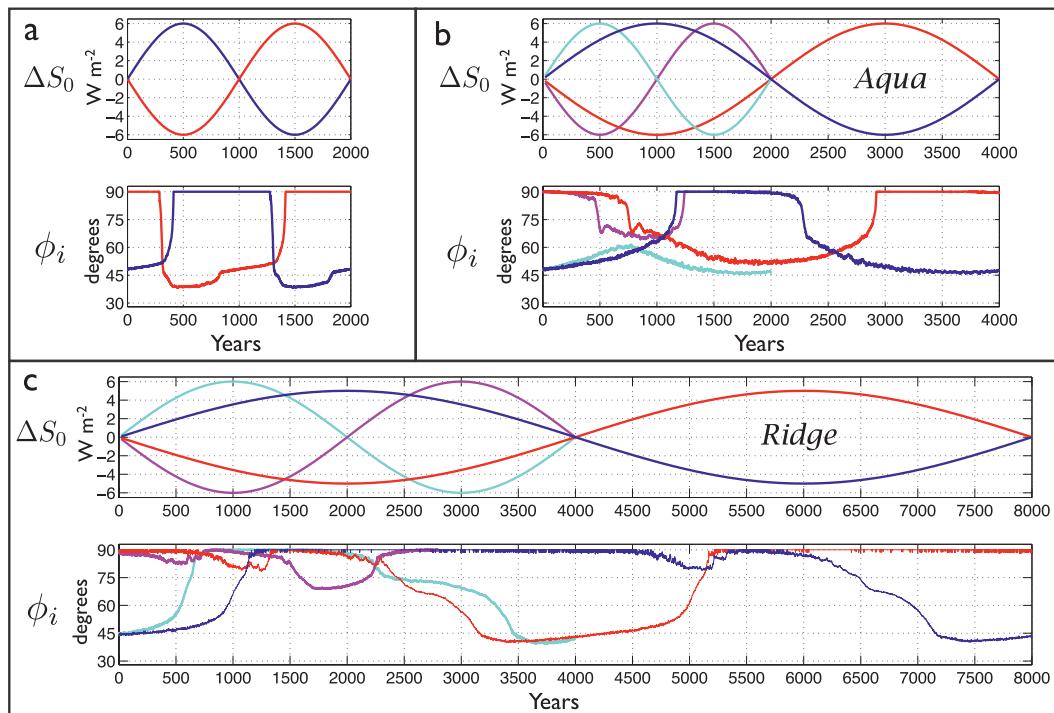
FIG. 2. Prescribed solar forcing and sea ice response in three different ocean configurations: (a) *Slab*, (b) *Aqua*, and (c) *Ridge*. The imposed variation in global-mean insolation (W m^{-2}) is plotted in the upper panel and the response of the sea ice edge (in terms of equivalent latitude ϕ_i) is plotted below: colors correspond to different initial conditions (Warm and Cold) and different amplitudes and periods of the forcing, as shown. In *Slab*, the OHT (q flux) is fixed to that of the Cold equilibrium state of *Aqua*, as described in FMR11. *Aqua* and *Ridge* both have fully interactive oceans.

FMR11), with periods of $L = 2000$, 4000, and 8000 yr (adjusting S_0 stepwise every 20 yr). Here S_0 is the most convenient control parameter to drive warming and cooling. These variations can be interpreted as proxies for any slow forcing on the global-mean energy budget, such as greenhouse gases or planetary albedo associated with growth and decay of continental ice sheets. Actual astronomical variations in S_0 are smaller. The Maunder Minimum reduction in solar luminosity is estimated at 0.2–1.4 W m^{-2} relative to present-day (Rind et al. 2004). Orbital eccentricity cycles drive about 1 W m^{-2} variation in S_0 at the 100-kyr scale due to changes in Earth–Sun distance (Loutre et al. 2004).

3. Hysteresis in sea ice cover

Figures 2a–c show imposed solar forcing and the resulting variations in sea ice extent in *Slab*, *Aqua*, and *Ridge*. As a convenient diagnostic for sea ice extent we use the "equivalent ice edge latitude" $\phi_i = \arcsin(1 - a_{ice})$, where a_{ice} is the fractional global ice area: ϕ_i transforms ice area to latitude units assuming zonal and interhemispheric symmetry of ice cover: as a global diagnostic, it filters out the seasonal cycle.

A complete hysteresis loop is simulated in all three configurations: the climate cools/warms between the reference Warm and Cold states by the time the forcing has returned to its initial reference value. Ice expands down to the midlatitudes ($\phi_i \approx 45°$) and retreats completely ($\phi_i = 90°$). The amplitude and period of forcing required for a complete warming/cooling cycle depends on the ocean configuration. We denote by ΔS_0 the maximum excursion of S_0 away from its reference value (the full range of forcing is thus $2\Delta S_0$). The runs presented in Fig. 2 result from a trial-and-error process to find the minimum ΔS_0 for full glaciation and deglaciation in each configuration, once a computationally feasible L was chosen.

a. Slab

Climate changes in *Slab* are nonlinear and switchlike: sea ice appears and disappears abruptly. $\Delta S_0 = 6$ W m^{-2} is sufficient to span the hysteresis loop. Without a deep ocean in *Slab*, there is very good time scale separation between the forcing ($L = 2000$ yr) and internal dynamics of the system, so the climate should be in quasi-equilibrium with the forcing. This is consistent with the fact that simulations initialized in Warm and Cold states

behave identically, simply phase-shifted by a half-period (red and blue curves in Fig. 2a).

Slab remains in a Cold, icy state for 1000 years (half period) for which S_0 spans 10 W m^{-2}. Sea ice retreats about 10° during this time (e.g., red curve in Fig. 2a, years 400–1400). This is consistent with arguments in FMR11: ice expansion is prevented by OHT convergence, which is invariant in *Slab* and peaks around 45°.

In FMR11, the Rose and Marshall (2009) EBM was fitted to *Aqua* and predicted unstable transition from Warm to Cold in response to a modest reduction in S_0. This is consistent with the abrupt sea ice growth in Fig. 2a. Although the transition is abrupt relative to the forcing time scale, it is not instantaneous: 30 years elapse between first appearance of sea ice and its reaching 50°. This is the most rapid change in any of our simulations.

The radiative damping time for a planet with a 30-m mixed layer is on the order of 2–3 yr (an *e*-folding time for the temperature response to a fixed radiative forcing).[3] Actual cooling rates in the GCM are an order of magnitude slower. However, the radiative forcing is set in part by the albedo anomaly of the advancing ice cap and is not fixed in time. Cooling proceeds through small persistent imbalances between outgoing longwave radiation (OLR) and absorbed solar radiation (ASR), both decreasing in near-equilibrium, introducing much longer lags into the system. TOA imbalance in *Slab* is roughly -2 W m^{-2} during the rapid cooling phase, consistent with a 15°C cooling over 30 yr with a 30-m slab ocean. Radiative imbalance is closer to 0.5 W m^{-2} throughout most of the simulation with excess OLR during the slow cooling and excess ASR during the slow warming as expected.

Even the very simplest albedo-feedback models exhibit such lags. For example, North et al. (1979) analyze finite-amplitude perturbations to a diffusive, spectrally truncated, one-dimensional EBM. From graphs of their solutions with typical earthlike parameters, one can infer global-mean radiative imbalances $O(1$ W m$^{-2})$ during the adjustment toward a stable moderate ice cap solution, implying a 60-yr cooling time. Large-scale climate change on scales of a decade and faster therefore seem improbable.

b. Aqua

In *Aqua* sea ice changes are switchlike only between roughly 70° and the pole. Equatorward of 70° ice advances and retreats much more gradually. As in *Slab*, there is little evidence of asymmetries between warming and cooling. The hysteresis loop is spanned by $\Delta S_0 = 6$ W m^{-2} for $L = 4000$ yr. With a shorter period ($L = 2000$ yr) this amplitude is too small to drive complete glaciation/deglaciation (cyan and magenta curves in Fig. 2b).

In the Warm state the polar oceans are strongly salt stratified with cool fresh surface water overlying salty warm water at depth (FMR11). The halocline is maintained by atmospheric moisture transport (net excess precipitation over evaporation) and polar easterly winds. Ekman pumping is downward everywhere poleward of a zero wind stress curl line at 65°. The halocline plays a key role in *Aqua* by isolating a large abyssal heat reservoir. The abrupt ice advance in both the red and magenta curves in Fig. 2b extends roughly to the equatorward edge of the salt-stratified region, and oceanic cooling over these first several centuries is largely confined to the upper few hundred meters of the polar oceans. In the red curve at year 800 ($\phi_i = 70°$), the deep water remains as warm as 12°C. It subsequently cools during the long, gradual ice expansion, but at the "glacial maximum" at year 2000 a pronounced halocline remains under the ice, and deep water does not cool below about 2°–3°C. In other words, *Aqua* retains some memory of the warm initial conditions after 2000 years of cooling.[4] The difference between the red and magenta curves in Fig. 2b shows that freezing over a salt-stratified water column is much easier than freezing over a temperature-stratified water column. Ice expansion beyond 70° in *Aqua* requires cooling the whole depth of the ocean, with consequently much higher effective heat capacity.

The Cold initial condition (blue curve in Fig. 2b) has no halocline; polar oceans under the thick ice cap are unstratified and near freezing (FMR11). By year 1000 the ice edge is near 65° and is underlain by a strong halocline, which develops gradually from sea ice melt. Warm water (4°–5°C) has intruded under the ice at intermediate depth (800 m). The abrupt melting is therefore preceded by significant warming under the developing halocline. However, ice loss appears to be driven by surface and lateral melt, rather than basal melt. The halocline probably delays the surface warming by allowing oceanic heat from lower latitudes to be stored at depth, rather than being trapped in a buoyant warm surface layer.

---

[3] Assuming OLR varies linearly with SST, with a radiative damping constant $B = 1.5$ W m^{-2} °C^{-1}.

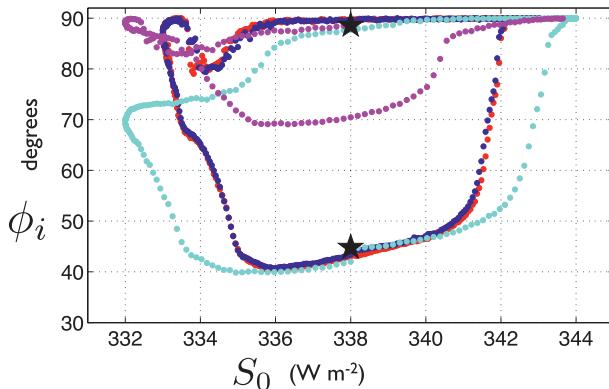[4] The deep polar oceans are below 0°C in the equilibrated Cold state of *Aqua* (FMR11).

FIG. 3. Hysteresis loops of sea ice edge vs solar constant in *Ridge*. The four model runs shown in Fig. 2c are plotted here with the same color conventions. The black stars indicate the equilibrium values from FMR11.

c. Ridge

We carried out longer simulations of *Ridge* with $L = 8000$ yr to improve the separation between oceanic and forcing time scales. The hysteresis loop is spanned by just $\Delta S_0 = 5$ W m^{-2} in this case, and the simulations initialized in Warm and Cold states behave very similarly with a half-period phase shift (red and blue curves in Fig. 2c). For shorter L a larger ΔS_0 is required to span the hysteresis. The cyan and magenta curves show simulations with $L = 4000$ yr and $\Delta S_0 = 6$ W m^{-2}; one undergoes the complete hysteresis (starting from the Cold state) while the other experiences only modest ice growth.

Figure 3 shows the same runs on a hysteresis plot of ϕ_i versus S_0. For reference we also plot the equilibrium values for the Warm and Cold states of *Ridge* taken from FMR11 (black stars). The two 8000-yr simulations (red and blue) trace out nearly identical hysteresis loops, and both pass through the equilibrium points at $S_0 = 338$ W m^{-2}. Figure 3 suggests that multiple states exist only within a narrow range of S_0 between 336 and 341 W m^{-2}.

In *Ridge* there is evidence of "sawtooth" asymmetry: warming and ice retreat tends to be faster than cooling and ice advance. Ice advance is also non-monotonic: a small ice cap first appears, then melts back before the main ice expansion occurs (seen in red, blue, and magenta curves). The transitions in *Ridge* are the most complex of the three model setups with many different time scales apparent in the evolution of the ice cover. The rest of the paper will focus on the red curve from *Ridge* in Fig. 2, which is initially ice free and goes through the full hysteresis over its 8000-yr period.

4. Details of the 8000-yr *Ridge* simulation

a. Sea ice

Figure 4 shows maps of sea surface conditions over the 8000-yr simulation. The shading shows ice thickness, based on a 20-yr average and plotted at its seasonal maximum (March). Colors indicate annual-mean sea surface temperature (SST). One hemisphere and polar cap are plotted; the climate is always roughly symmetric about the equator in the annual mean.

The initial small ice cap is well established by year 1000 and is gone by year 1400. This ice is thin and seasonal. Poles then remain largely ice free until about year 2400, after which perennial sea ice appears. The ice cap grows in extent and thickness over the following 800 yr; it has a pronounced zonal asymmetry with thicker ice on the western edge of the basin. Year 3100 is a time of rapid ice expansion, particularly on the eastern side of the basin; by year 3200 the ice has reached its maximum extent and is nearly zonally symmetric. At year 4000, when S_0 has returned to its reference value, the climate remains cold and glacial.

The ice cap retreats slowly and symmetrically between year 3500 and 4500. Zonal asymmetry reappears around year 4600. A rapid period of asymmetric ice melt follows, and finally a relatively abrupt complete ice melt after year 5000. The remaining 3000 years of the simulation, while S_0 is above its reference value, are ice free. There is no return to a seasonal ice regime like the initial small ice cap.

b. Adjustment of atmosphere and planetary energy balance

Figure 5 gives time series of key quantities in the planetary energy balance (all annual, zonal means). Global-mean surface air temperature spans 24°C (Fig. 5a). Temperature changes are polar amplified by a factor of 2. Albedo feedback is clearly acting to amplify climate changes, as sea ice extent is imprinted starkly on TOA albedo (Fig. 5b).[5] While the ultimate driver of the climate changes is the ± 5 W m^{-2} variation in S_0, the ASR time series does not resemble the sinusoidal variation of insolation. Absorbed solar radiation is slaved to the ice extent and spans 25 W m^{-2} (Fig. 5c). Global-mean OLR is tightly coupled to ASR throughout, as

---

[5] TOA albedo is computed as 1 minus the ratio of annual-mean ASR to annual-mean insolation. Surface albedo is the ratio of up-welling to downwelling surface shortwave fluxes. Polar TOA albedo increases by 0.2 during glaciation, a factor of 2 smaller than the surface albedo change, due primarily to clouds (FMR11). Donohoe and Battisti (2011) found a somewhat larger damping (factor of 3) in phase 3 of the Coupled Model Intercomparison Project models.
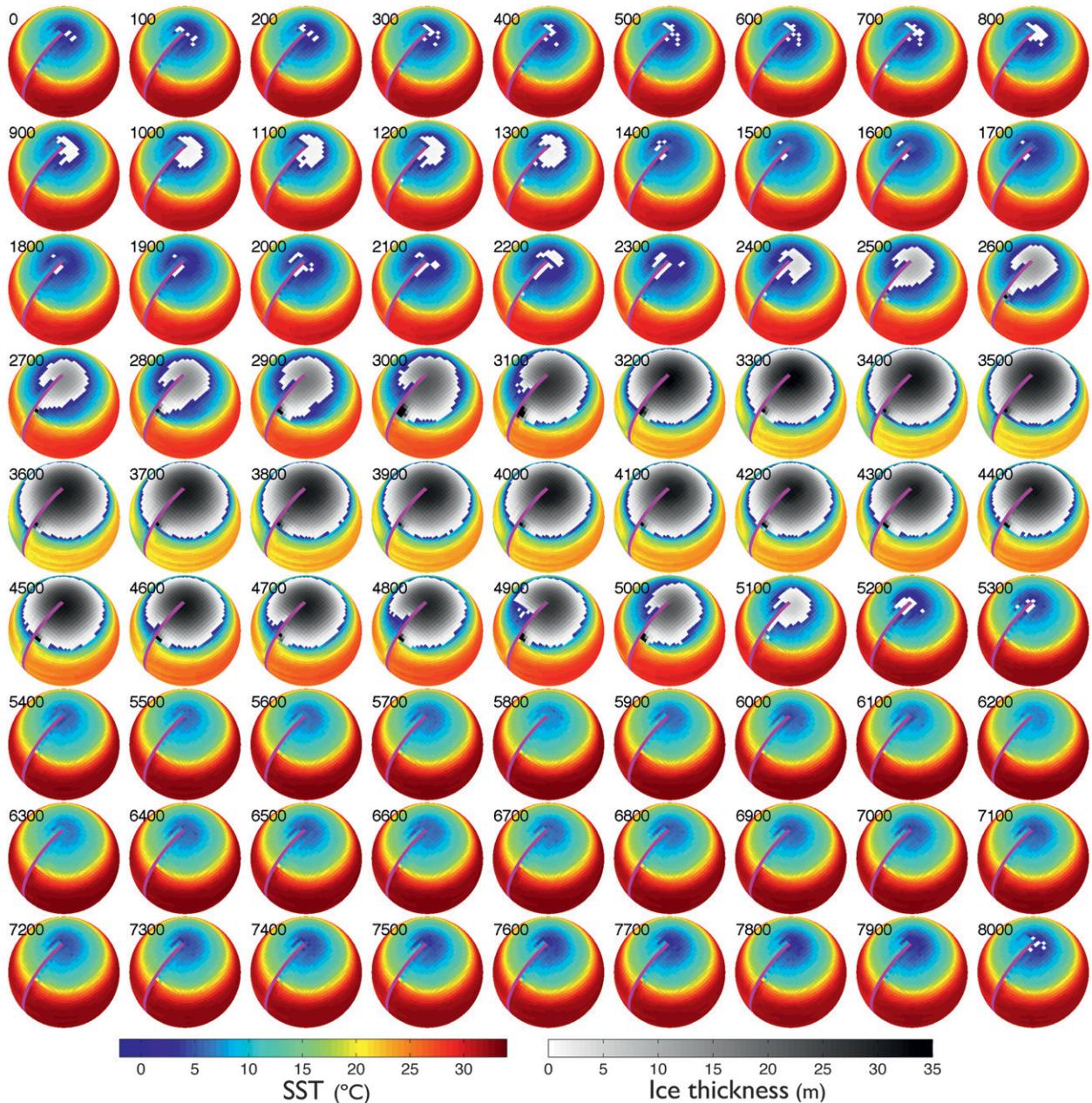
FIG. 4. Evolution of sea surface conditions over the 8000-yr *Ridge* simulation. The frames are 20-yr averages every 100 years. Colors indicate annual-mean SST; shading indicates combined sea ice plus snow thickness at its maximum seasonal extent in March (Northern Hemisphere). Ice thickness is plotted where sea ice concentration exceeds 30%.

surmised above in the context of adjustment times in *Slab*.

Both atmospheric heat transport (AHT) and ocean heat transport (OHT) increase in the cold icy climate (Figs. 5d and 8). Total heat transport (THT) is tightly coupled to ice extent and is largest at the glacial maximum. There is a regime shift in the thermal stratification of the atmosphere between the Warm and Cold states

(measured in terms of a vertical gradient in moist potential temperature, Fig. 5e), also tightly coupled to the appearance/disappearance of sea ice. The polar thermal stratification varies between a nearly moist-neutral convectively adjusted state (during ice-free intervals) and a highly stratified state (during icy intervals).

Figure 5f shows the energy budget of the polar region (averaged north of 70°N). Polar ASR is quantized into
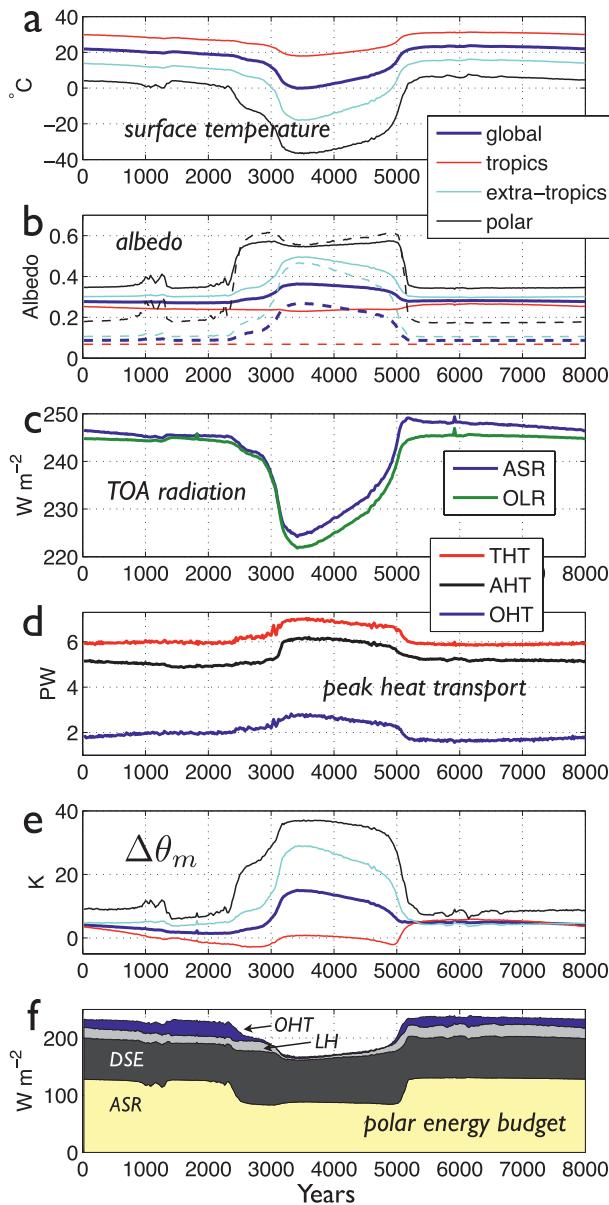
FIG. 5. Evolution of the planetary energy balance over the 8000-yr *Ridge* simulation (all zonal, annual-mean quantities). (a) Surface air temperature, averaged globally (thick blue), equatorward of 30° (red), poleward of 30° (cyan), and poleward of 70° (black). (b) Albedo at TOA (solid lines) and surface (dashed); same area averaging as above. (c) ASR and OLR (global means). (d) Peak values of THT, AHT, and OHT (note these are not additive since they peak at different latitudes). (e) Atmospheric thermal stratification computed as θ_m (500 hPa) minus θ_m (surface), where θ_m is moist potential temperature. (f) Components of the polar energy budget (poleward of 70°): ASR (yellow), dry and latent components of AHT convergence (gray), and OHT convergence, plotted as an additive stack. The total balances the polar OLR.

ice-free/icy states: about 130 versus 85 W m^{-2}. OHT convergence switches abruptly from roughly 15 W m^{-2} during ice-free periods, to 25 W m^{-2} following the collapse of the initial small ice cap, to near zero with perennial ice, and returns to 15 W m^{-2} as the ice disappears. Polar AHT convergence first increases while ice is expanding and then decreases during the full glacial. The latent heat (LH) component goes to zero as extreme cold precludes any significant water vapor at the poles. The dry static energy (DSE) component also diminishes somewhat during the glacial maximum. Total AHT convergence reaches a minimum of 76 W m^{-2} around year 3500, well below the roughly 100 W m^{-2} in the present-day Arctic (Overland and Turet 1994; Serreze et al. 2007; Porter et al. 2010). This decrease occurs in spite of increased AHT at its midlatitude peak (Figs. 5d and 8), consistent with the large equator-to-pole temperature gradient. In the full glacial state, the midlatitude storm track is tied to the strong baroclinic zone at the ice edge, and the poles are isolated from the intense heat fluxes occurring at midlatitudes. The poles therefore get very cold and the sea ice becomes very thick, around 30 m or so.

In summary, all aspects of the planetary energy balance are slaved to the size of the sea ice cap. The key question is what sets the sea ice extent and time scales for advance/retreat.

c. Ocean circulation

Wind stress is shown in Fig. 6a. Both zonal stress τ_x and Ekman pumping $w_{Ek} = \nabla \times [\boldsymbol{\tau}/(\rho_o f)]$ increase in magnitude in the subtropics as the climate system enters the full glacial state around year 3000. There is a modest decrease in the Ekman suction driving the subpolar gyres. Spatial structure of τ_x is plotted in Fig. 7 as anomalies from the Warm state. The Cold state features stronger trades and weaker polar easterlies (FMR11). A transient equatorward shift in the westerlies occurs during the cooling.

Gyre circulations are plotted in Fig. 6b in terms of maxima of the barotropic mass transport ψ_{horiz}. The subtropical gyre scales directly with subtropical w_{Ek}, as expected from Sverdrup balance: there is a 20% increase in mass transport around year 3000. Subpolar gyre transport decreases somewhat during the glacial interval.

In Fig. 8 we plot several snapshots of MOC and heat transport to illustrate their spatial structure and variability. MOC is plotted in terms of the residual-mean overturning streamfunction ψ_{res}. One hemisphere only is plotted, as the circulation is always roughly symmetric about the equator. These plots use a stretched depth axis to reveal the upper-ocean structure of ψ_{res}. The
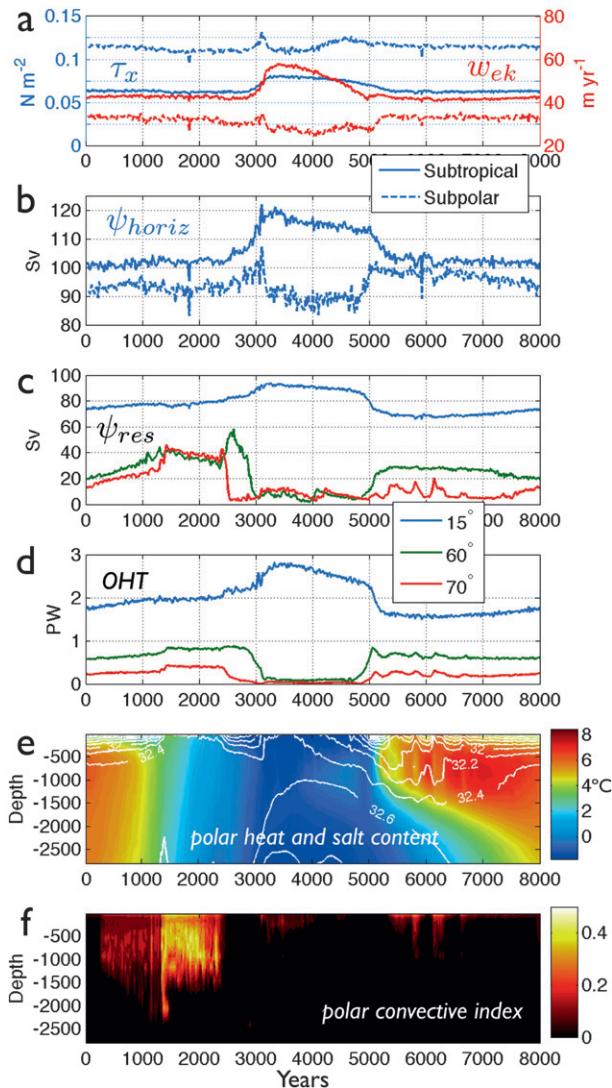
FIG. 6. Ocean circulation in the 8000-yr *Ridge* simulation (all zonal, annual-mean quantities). (a) Zonal wind stress τ_x (blue) and Ekman pumping/suction w_{Ek} (red) at their subtropical (solid) and midlatitude (dashed) extremes (all plotted as absolute values). (b) Horizontal transport by subtropical (solid) and subpolar (dashed) gyres (absolute values), calculated as extrema of the barotropic streamfunction ψ_{horiz}. (c) Transport by MOC at 15°, 60°, and 70° (defined as maximum of residual-mean overturning streamfunction ψ_{res}). (d) Net poleward ocean heat transport across the same latitude bands. (e) Depth–time cross sections of potential temperature (colors) and salinity (white contours in intervals of 0.2 psu) of polar oceans averaged north of 70°. (f) Convective index at the pole vs depth, indicating the frequency of convective mixing.

low-latitude MOC is a shallow wind-driven subtropical cell (STC) (Klinger and Marotzke 2000) extending no deeper than about 500 m and always present throughout the simulation. At higher latitudes the MOC extends to much greater depth but varies substantially, disappearing entirely in the glacial state (e.g., year 4000 in Fig. 8).
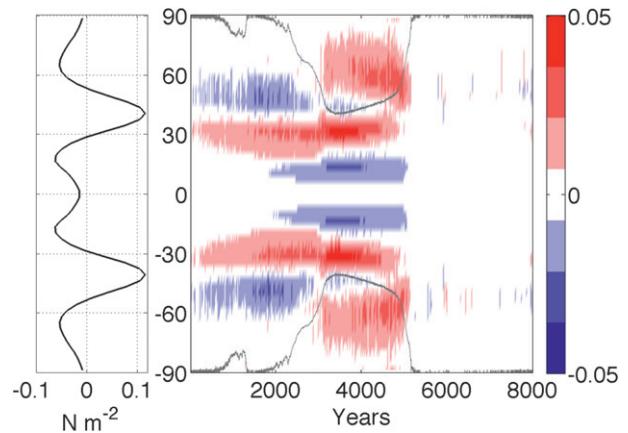

FIG. 7. Zonal wind stress τ_x (zonal mean) in *Ridge*: (left) the time-mean stress in the Warm ice-free state and (right) τ_x anomalies as a function of latitude and time (colors; N m^{-2}). The ice edge latitude ϕ_i is overlain in gray for reference (reproduced from Fig. 2c).

Time series of the column maxima of ψ_{res} are plotted in Fig. 6c at representative latitudes (roughly 15°, 60°, and 70°). The shallow subtropical MOC (blue curve) scales with the easterly trade wind stress τ_x (Fig. 6a) and increases during the glacial interval. At higher latitudes variations in MOC are highly nonlinear, first increasing throughout the ice-free cooling phase and then collapsing abruptly coincident with appearance of sea ice (green and red curves in Fig. 6c). As can also be inferred from the snapshots in Fig. 8, the MOC collapses first near the pole (year 2500), then later in midlatitudes during transition to the full glacial state (year 3000). It resumes during deglaciation, with some variability at high latitudes.

Figure 6d shows OHT across the same latitude bands (see also Fig. 8). The changes from warm to cold climate are of opposite sign in low and high latitudes. OHT out of the tropics increases from 2 to 3 PW as climate cools. This change scales well with τ_x and the subtropical ψ_{res}. Stronger easterly trade winds drive more upwelling of cold water near equator, although much of the increase is due to larger temperature contrast across the overturning cell as the deep water cools, as argued by FMR11. OHT at mid-to-high latitudes also scales with ψ_{res}, collapsing as ice advances and resuming as ice retreats. There is little evidence that OHT scales with w_{Ek} in the subpolar gyre, as assumed by Rose and Marshall (2009).

Cross sections of polar thermohaline stratification are shown in Fig. 6e (potential temperature and salinity averaged north of 70°N), and the depth and frequency of polar convection is plotted in Fig. 6f. A stable polar halocline is present initially, similar to that discussed above in *Aqua* but less intense: cool fresh surface water
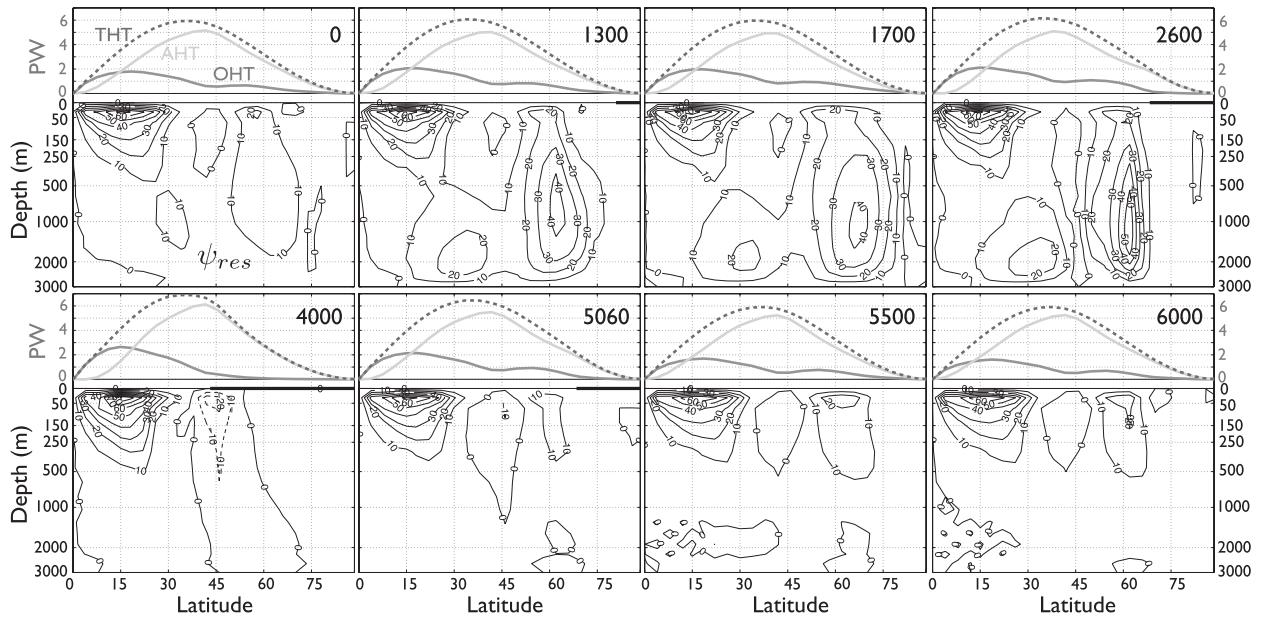
FIG. 8. Snapshots of ocean circulation and meridional heat transport from the 8000-yr *Ridge* simulation. Each panel shows one hemisphere only, based on a 20-yr mean beginning at the indicated year. Upper section of each panel shows heat transport (PW) by the ocean (gray solid) and atmosphere (light gray solid): total (dashed). Bottom section shows residual-mean overturning streamfunction ψ_{res} (black; 10-Sv contour interval), with ice cover indicated by the thick black line at the surface. The vertical depth coordinate is stretched to emphasize upper-ocean structure.

overlies warmer saltier water (difference of 1.4 psu). As in *Aqua*, this allows polar ice to form at year 1000 while deep water remains well above freezing (4°–5°C). Some vertical mixing occurs in the polar oceans despite the halocline, beginning around year 200 and penetrating progressively deeper for 1000 years (Fig. 6f). The deep heat reservoir and upper-ocean halocline are slowly eroded. Brine rejection from the growing ice cap likely accelerates this destabilization after year 1000. Around year 1300 the halocline and the ice abruptly vanish. Surface temperatures rise above freezing, and polar oceans remain unstratified for 1000 years while S_0 decreases. Intense deep convection begins concurrently with the loss of ice and stratification, driven by surface heat loss. This period of unstratified, convecting polar oceans is associated with maxima in polar MOC and heat transport (Figs. 6c,d and 8). After the halocline is lost, the polar ocean is weakly stratified by temperature (colder water at depth) and cannot freeze over before mixing out its deep heat reservoir. Perennial ice appears after another 1000 years of cooling.

A halocline reforms during the period of ice growth around year 2500, driven by an increase in net precipitation in the polar regions during this interval (inferred from the increase in latent heating in Fig. 5f). The poles stay warm enough to allow significant precipitation, and the ice surface reaches the melting point every

summer, injecting fresh meltwater into the ice-covered oceans. The transition to full glaciation shuts off both precipitation and seasonal melt while also injecting brine from thickening ice; the halocline consequently disappears again. It reappears during deglaciation, helped by meltwater from thinning ice.

After deglaciation the halocline oscillates with a period of about 500 yr. Unstratified intervals feature polar convection, active high-latitude MOC, increased OHT across 70°, and warmer poles; stratified intervals have no convection, no MOC, reduced high-latitude OHT, and colder poles (variations of about 1.5°C). The impact on global climate is small (<0.5°C in global-mean surface temperature), but they are reminiscent of the "deep decoupling oscillations" of Winton and Sarachik (1993). Oscillations end after year 6500, and the system drifts back to the stable halocline characterizing the equilibrated Warm state.

These zonally averaged plots mask considerable cross-basin asymmetry in *Ridge*. Deep-water formation tends to be localized along the eastern margin due to advection of relatively warm, salty water by the subpolar gyre (evident in SST and sea ice extent in Fig. 4). These asymmetries, which are absent from *Aqua*, bring our idealized model one key step closer to reality and likely contribute to the richer dynamics found in *Ridge* (Fig. 2).
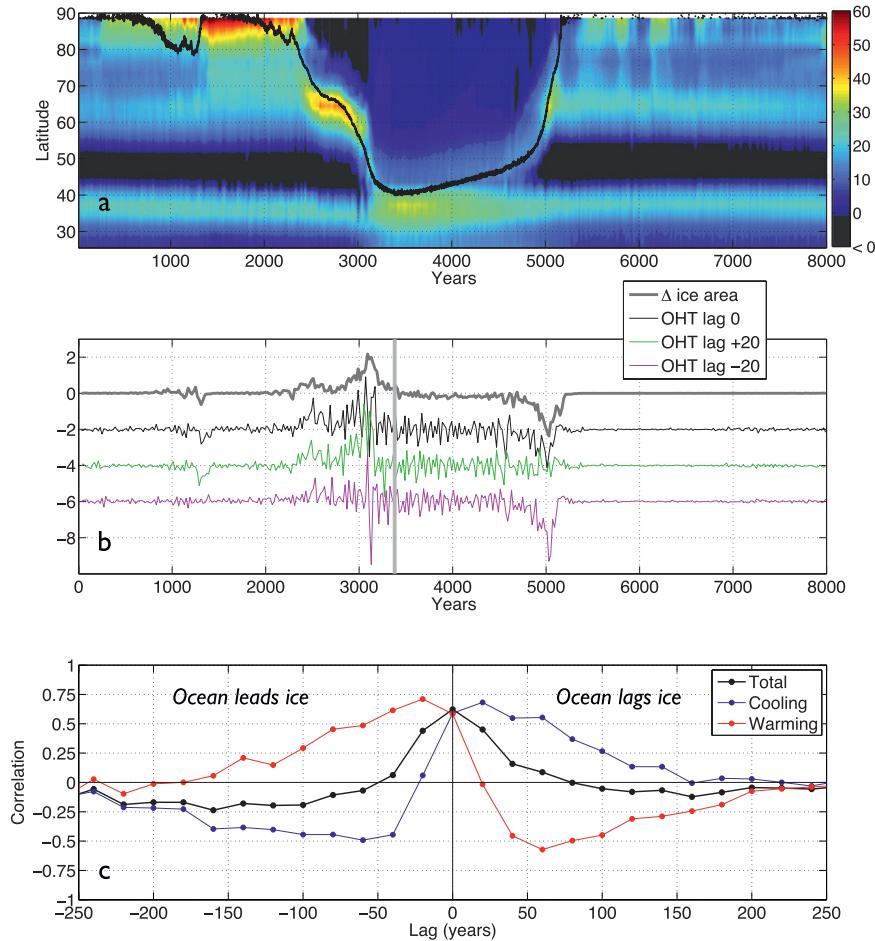
FIG. 9. Coevolution of OHT convergence and sea ice extent in *Ridge*. (a) Zonally averaged OHT convergence (W m^{-2}) poleward of 30°N, with ice edge latitude ϕ_i overlain in black. (b) Rate of change of sea ice extent (thick gray line) plotted as percent change in global surface area per 20-yr interval. Other curves are lagged changes in OHT convergence in the vicinity of the ice edge [see text; 10^{14} W (20 yr)$^{-1}$], offset by -2, -4, and -6 for convenience. (c) Correlations between changes in ice area and lagged OHT convergence changes as function of ocean lag. Black: full time series; blue: just the first 3400 yr; red: just the final 4600 yr.

d. Ocean heat transport and sea ice

Figure 9a is a time–latitude plot of zonal-mean ocean heat transport convergence, overlain with the ice edge latitude ϕ_i. The spatiotemporal pattern of OHT convergence is complex, but intimately related to the ice edge. Three different latitude bands per hemisphere tend to experience significant dynamical heating: the poles (80°–90°), the subpolar oceans (60°–70°), and the subtropical oceans (35°–40°). This meridional structure is dictated by wind forcing and gyral circulation in *Ridge*, which are relatively constant and robust. However, the heating rates vary greatly with size and tendency of the ice cap, with maxima just equatorward of the ice edge during cooling (e.g., the poles at year 1500, subpolar

oceans at year 2800). Heating rates are near zero everywhere poleward of the ice edge.

Does the ice cap expand and contract in response to changes in the ocean heating or does the ice edge dictate the OHT convergence (e.g., by setting the location of ocean convection)? Lead–lag correlations between time series are often used to infer causality in complex systems. The challenge here is that OHT convergence is spatially complex, involves significant zonal asymmetries, and is only partly related to changes in the ice edge. In Fig. 9b we construct time series of changes in ice area a_{ice} and OHT convergence in the vicinity of the ice edge at various lags, as follows: 20-yr mean model output is used to define temporal variations in ice extent. An area mask outlining the marginal ice zone is computed by

finding all grid points with nonzero change in a_{ice} for each 20-yr interval. The change in OHT convergence within this limited area is then computed for a range of lagged 20-yr periods. Figure 9b shows the change in a_{ice} as well as the area-masked OHT convergence at lags −20, 0, and +20 yr. No assumptions of zonal symmetry are made here. Time series in Fig. 9b are positive where the masked OHT convergence decreases (i.e., we plot −1 × the time derivative of the convergence). To the extent that changes in the ice edge are dictated by the ocean, we should expect positive correlation with the ocean leading the ice.

Lagged correlation is plotted in Fig. 9c. For the entire time series (black) correlation peaks at lag 0, meaning that changes in OHT convergence occur simultaneously with changes in a_{ice} (as resolved by 20-yr averages), making inferences about causality difficult. A clearer picture emerges when correlations are computed separately for the cooling and warming phases (divided at year 3400): a peak correlation of +0.7 shifts from positive to negative lag.

The blue curve in Fig. 9c shows correlations for the cooling phase (first 3400 yr). OHT convergence near the expanding sea ice margin[6] tends to increase before the expansion (negative correlations at negative lags), and then decrease after the ice expansion (positive correlations at positive lags). This is consistent with a passive role for ocean circulation and ocean heat transport during the cooling period. Convection at the advancing ice edge drives a substantial MOC that delivers heat and slows down the advance. Once this process has exhausted the local deep heat reservoir, ice is able to expand and curtail the surface heat fluxes driving the convection. OHT shuts down because the sea surface freezes over, not the other way around.

The red curve is computed from the warming phase (final 4600 yr) and shows the opposite pattern. Poleward ice retreat tends to be preceded by an increase in OHT convergence (positive correlation at negative lag) and is followed by a decrease in OHT convergence (negative correlation at positive lag). We infer a more active role for the ocean circulation during the warming process. The ocean heating that precedes ice retreat serves to thin the ice cap, preconditioning it for a more rapid retreat. The subsequent decrease in OHT convergence in the region formerly occupied by the ice margin can be understood in terms of a poleward shift in the oceanic convection and heating, following the ice edge. OHT convergence is tightly coupled to the sea ice edge in both warming and cooling phases.

5. Discussion

We impose a radiative forcing with a single frequency on a coupled GCM and find many different shorter time scales in response. Some aspects are abrupt—in the sense that changes occur on time scales much faster than the forcing and are clearly mediated by internal out-of-equilibrium dynamics. Abruptness is found in both warming and cooling responses of all three of our configurations (*Slab*, *Aqua*, and *Ridge*). In *Ridge*, the peak global-mean warming and cooling rates are both about 6°C $(100 \text{ yr})^{-1}$ (year 3100 and 5000, respectively). Overall, *Ridge* exhibits a sawtooth pattern of climate change with cooling and ice expansion occurring more slowly than warming/ice retreat (Fig. 2c). Note, however, that the most abrupt regional changes in the ocean actually occur during the cooling and are associated with the collapse of deep-water formation after the sea surface freezes over (e.g., the MOC indices in Fig. 5c). Potential implications for interpreting the paleoclimate record are discussed below.

We emphasize that changes in MOC and OHT are not monotonic in latitude: they have different signs at low and high latitudes, resulting from two somewhat independent processes. The low-latitude circulation is wind driven, takes heat off the equator, and moves it poleward. This circulation intensifies in an icy climate, with ocean heat transport affected by increases in both wind-driven mass flux and temperature contrast between surface and abyssal waters. FMR11 showed that enhanced OHT into midlatitudes stabilizes the large ice cap at equilibrium. The role of OHT in the equilibrated Warm state is more subtle (Rose and Ferreira 2013). Direct OHT convergence at the poles is small, except during transient cooling.

The freshwater hosing scenario for rapid cooling invokes a shutdown of the high-latitude MOC as a prerequisite for sea ice expansion. In *Ridge* we find a superficially similar situation—MOC does indeed shut off when ice is present—but the causality is quite different. The high-latitude MOC and associated OHT depend on thermohaline convection. In the equilibrium Warm state, the polar oceans are salt stratified and high-latitude MOC is weak. Convection and MOC switch on only when the climate is cooling and, as argued above, act to slow down the cooling. This is a passive response of the ocean to the radiative forcing and is a negative feedback: cooling the ocean destabilizes it, leading to mixing and the gradual, slow depletion of the deep heat reservoir. This confirms speculation by

---

[6] Changes in a_{ice} are not strictly positive: this period includes the collapsing small ice cap at year 1400.

Marotzke and Botzet (2007), who found a much more extreme transient MOC increase in coupled simulations under total darkness (zero insolation), but suggested that enhanced deep circulation ought to occur in more moderate cooling scenarios. Once ice does form, it insulates the sea surface, arresting the cooling process and restratifying the water column. The site of deepwater formation, mixing, and heat release then shifts equatorward with the ice edge. There is no evidence here for Stommel-type bifurcations. The MOC does not collapse because of thermohaline forcing; rather, it is driven by cooling and collapses because sea ice insulation stops the cooling. The only real threshold behavior here seems to be in the ice—both albedo and insulation effects.

Previous works have found very active roles for sea ice in glacial climate variability, particularly in simulations with simplified Earth System Models of Intermediate Complexity (EMICs). Wang and Mysak (2006) found self-sustaining DO-like oscillations and argued that brine rejection (and its effects on upper-ocean buoyancy) was an essential part of the mechanism. Loving and Vallis (2005) found weaker MOC in colder climates with more extensive sea ice cover (with deepwater formation shifted equatorward with the ice edge), arguing that the ice-induced insulation of the sea surface is a necessary condition for weakening the MOC. Weakened MOC in turn destabilizes the system, giving rise to intermittent millennial-scale oscillations in their model. We have not found an analogous oscillatory regime (aside from the transient warm oscillations following deglaciation in *Ridge*). However, our results do confirm the close coupling among sea ice, upper-ocean buoyancy, and MOC. We also employ a substantially more complex model than these previous works (global domain, fully coupled primitive equation models for both atmosphere and ocean, dynamically consistent hydrological cycle, and wind stress).

From Fig. 2, the ΔS_0 required for a complete glaciation/deglaciation cycle depends on the forcing period L. In *Aqua*, for example, 6 W m^{-2} is insufficient at $L = 2000$ yr but sufficient at $L = 4000$. This raises the possibility that even weaker forcings, varying over sufficiently long periods, could trigger very large climate changes. In *Ridge*, 5 W m^{-2} is sufficient at $L = 8000$ yr whereas 6 W m^{-2} is only marginally sufficient at $L = 4000$ yr, depending in this case on initial conditions. Starting from the Warm state (magenta curve in Fig. 2c) yields only modest ice growth down to 70°, whereas full deglaciation (and reglaciation) occurs when initialized in the Cold state (cyan curve in Fig. 2c). The cold climate is thus more sensitive and more variable than the warm climate, also a notable feature of the long-term paleoclimate record (e.g., Zachos et al. 2001). We can

understand this difference here as arising from the basic asymmetry of sea surface heating: warming stratifies the water column while cooling destratifies it and encourages mixing. It is therefore possible to deglaciate without warming the entire depth of the ocean. The effective heat capacity for surface cooling is greater than for warming. A similar conclusion was reached by Stouffer (2004) on the basis of coupled GCM simulations with altered greenhouse gases.

To what extent are these transitions influenced by the existence of multiple equilibria? With sea ice and other nonlinear mechanisms present, one might expect a nonsinusoidal response to a sinusoidal forcing even without any hysteresis in the system. The multiple equilibria do, however, shape these transitions in several interesting ways. First, the hysteresis by definition means that the climate undergoes "irreversible" climate change under a transient forcing. A temporary (but sufficiently long lived) increase in greenhouse gases or solar forcing can lead to permanent loss of sea ice in this model. No such hysteresis was found by Armour et al. (2011) as CO_2 was first raised then lowered in a comprehensive coupled GCM [Community Climate System Model, version 3.0 (CCSM3.0)] with realistic geography. This discrepancy may simply be due to the geometry of the models (stronger sea ice feedbacks on an aquaplanet) or may point to important intermodel differences in various radiative feedbacks, and perhaps deficiencies in our simplified atmospheric physics. Alternatively, there may be no true discrepancy at all. Armour et al. simulate a relatively fast adjustment process that engages only the upper few hundred meters of the ocean. Our shorter simulations (e.g., magenta curves in Figs. 2b and 2c) behave similarly. Evidence for bifurcations or "tipping points" associated with the loss of Arctic sea ice in comprehensive GCMs has been equivocal; for example Winton (2006) found such evidence in one model (ECHAM5) but not another (CCSM3.0) under quadrupled CO_2. Eisenman (2012) reviews the spectrum of different GCM behaviors and shows how it can be replicated in a simple column model for the Arctic energy budget by varying several key parameters, particularly those controlling seasonal ice thickness and ocean temperature. Our warmings fit the Eisenman "Scenario III": unstable shift from perennial ice to completely ice free, without passing through a stable seasonal ice regime.

By definition, a stable equilibrium lies within a basin of attraction in the phase space of a dynamical system. Our GCM will adjust toward one or other of the stable states (Warm and Cold) with some characteristic time scale once the climate is "close enough" to the equilibrium. We have not attempted to quantify these thresholds but find evidence for them in Fig. 2, where the approach

toward stable states is somewhat independent of the instantaneous forcing phase. In *Aqua* rapid ice loss and warming occurs when S_0 is large and increasing (red curve, year 2900), large but decreasing (blue curve, year 1150), and small and increasing (magenta curve, year 1200). There is no simple one-to-one relationship between instantaneous forcing and response. This may be significant for understanding glacial cycles and orbital forcing. If such cycles involve adjustments between stable equilibria (e.g., Paillard 1998), then one might find summer insolation at 65°N increasing during some glacial inceptions while decreasing during others, with no inconsistency. Milankovich cycles contain many different time scales; it may be difficult or futile to correlate instantaneous variations in insolation with climate, even if solar forcing is the ultimate driver.

The Warm and Cold aquaplanet states bracket our current climate, and the model passes through a more earthlike state during the transitions. In *Ridge* this occurs between years 2500 and 3000, with perennial but thin and asymmetric sea ice. Polar temperatures are much warmer than at the glacial maximum due to strong AHT, and ice thickness is limited by summer melt. In the ocean a strong MOC extends to subpolar latitudes, with associated OHT convergence preventing (or delaying) rapid ice expansion. There is a vigorous subpolar gyre and deep-water formation on the eastern edge of the basin. All of these features are found qualitatively in the present-day climate. It is notable that the transitions in *Ridge* tend to "slow down" when passing through this more earthlike climate (Fig. 2c).

Our study was motivated in part by interest in DO events and abrupt glacial climate change. Analogies can be drawn between our results and both DO event cycles (millennial scale) and glacial cycles (100-kyr scale). These analogies are far from perfect but may be useful. We outline both in turn, followed by some shortcomings of the aquaplanet framework.

The sawtooth pattern of climate change is found in the paleoclimate record at multiple time scales—characteristic of both DO events and the Late Pleistocene glacial/interglacial cycles (see, e.g., Fig. 1 of Clement and Peterson 2008). In *Ridge*, this asymmetry is fundamentally related to the destabilization of the water column during cooling and ice formation, which draws up heat from below and drives a vigorous ocean circulation. Again, the effective heat capacity is greater during cooling than warming, as found by Stouffer (2004).

While the warmings in our coupled models are abrupt, they are slower than observed for DO events [a few decades at most; Seager and Battisti (2007)]. It is not clear why our *Slab* model, which is devoid of ocean physics, produces the most realistic rapid warming time scale. On the other hand, the coupled model does seem to correctly reproduce the seasonality of abrupt warming. Seager and Battisti argue that the largest-amplitude temperature changes in the North Atlantic occurred in winter, estimated at 20°–30°C. In *Ridge*, the most rapid change in regional and seasonal temperatures is also the winter warming of the high latitudes during deglaciation: we find January warming as high as 27°C $(100 \text{ yr})^{-1}$ at 60° latitude when sea ice retreats off the subpolar gyre. This good fit does not imply that we are simulating the correct underlying mechanism, but it does imply that DO events are consistent with rapid retreat of sea ice cover (Li et al. 2005, 2010). We have also noted meridional shifts in ocean convection and deep-water formation following the ice edge. Glacial climate variability is associated with analogous shifts in NADW formation (Rahmstorf 2002).

High-latitude haloclines are also relevant to DO events. Li et al. (2010), citing unpublished data from Dokken et al., outline a DO cycle scenario with alternating build-up and erosion of a fresh halocline in the Nordic seas. The halocline allows sea ice to expand southward while the underlying ocean slowly warms from northward ocean heat transport. Eventually this deep warming destabilizes the water column; abrupt ice melt and surface warming ensues. There is an obvious connection between this scenario and the abrupt disappearance of the small ice cap in *Ridge* around year 1400. Also, *Aqua* and *Ridge* both feature ocean warming at intermediate depth (isolated by a near-surface halocline) in advance of deglaciation. A plausible reason for our relatively slow "abrupt" warmings is the lack of ocean topography. Extensive continental shelves and ridges in the Nordic seas would likely constrain oceanic warming to shallower depths, reducing the effective heat capacity involved in these transitions.

On the other hand, our transitions involve huge global climate changes (20°C global-mean surface temperature changes in *Ridge*) that are akin to exaggerated glacial/interglacial cycles. The shift from the Last Glacial Maximum to present climate is estimated at 5°C (Braconnot et al. 2007) and major changes in sea ice extent (de Vernal and Hillaire-Marcel 2000). Glacial cycles, like our simulations, are paced by well-defined oscillatory radiative drivers (e.g., Roe 2006; Huybers 2011), although Milankovich forcing primarily affects seasonal and meridional distribution of insolation rather than global annual-mean S_0. In both cases the response to the forcing is nonlinear. Amplifying or resonance mechanisms are needed to account for both the 100-kyr time scale (e.g., Tziperman et al. 2006) and the "sawtoothness" of the global ice volume record (e.g., Imbrie et al. 1984; Huybers and Wunsch 2004).

Other aspects of our work correspond to neither DO events nor glacial cycles. The geometrical simplicity of our setup limits comparison with past climates. Our S_0 variations are contrived as the minimal forcing to span the hysteresis loop and are not based on any known events. We do not include an interactive carbon cycle, a key amplifying feedback on glacial time scales that would presumably reduce the minimum ΔS_0. The lack of continents may affect many aspects of the response. Although this has not been quantified, we presume that all sea ice feedbacks are stronger on aquaplanets, simply because of the greater surface area. This includes albedo feedback as well as the coupling of sea ice and MOC. Another caveat concerns time scales: In glacial climates, the longest memory (heat capacity) is probably in the ice sheets, while in the aquaplanet (with ice sheets replaced by sea ice) the ocean carries most of the memory. Our model also treats cloud and boundary layer processes crudely relative to standard AGCMs, and it is unknown to what extent this biases our results.

Despite these caveats, what aspect of this work might be helpful in the interpretation of the paleoclimate record? The key result concerns variations in MOC and associated heat transport. It seems inevitable that a large-scale cooling and ice expansion be accompanied by a marked change in high-latitude ocean circulation. As discussed in the introduction, it is commonly assumed in the paleoclimate literature that the ocean is the primary driver of such changes. We have shown that the opposite can also occur: our MOC changes are a passive response to sea ice variations (at least in the cooling phase), which are themselves forced from above by solar radiation and albedo feedback.

Does this leave a testable prediction? In principle, yes, given proxies of deep-water formation rate coincident with a climatic cooling. If cooling is driven by radiation (as in our simulations) deep-water formation ought to increase in advance of the cooling. On the other hand, if the "hosing" scenario is at work, then the proxies should decrease in advance of the cooling. In practice this would require dating of proxies to within 100 years (based on correlation times in Fig. 9c). This does not seem at all promising given current dating uncertainties in marine sediments; for example, reconstructions of MOC based on ^{231}Pa/^{230}Th ratios are limited by a 500-yr response time to circulation changes (McManus et al. 2004). The takeaway message must therefore be one of "correlation does not imply causality."

Finally, before concluding, we urge caution in drawing global inferences about ocean circulation and OHT from proxies tied to specific locations. Figures 6–9 show that spatial patterns of variability are complex, even in a model with very simple boundary conditions and a single

smooth forcing. The sign of changes in OHT, and the abruptness with which it changes, depends very much on where in the ocean one is looking. OHT emphatically does not have a single well-defined spatial pattern that switches on and off with climate change; it varies in complicated ways that depend intimately on the current state of the system.

6. Conclusions

We summarize our main conclusions as follows.

1) Hysteresis and abrupt transitions between ice free and cold, glacial conditions are initiated in a fully coupled aquaplanet climate model by fairly modest, slow forcing. Transitions are forced by variations in global-mean insolation and albedo feedback.
2) Variability in the ocean's MOC and associated heat transport is largely a passive response to changes in sea ice extent. Particularly during cooling and ice expansion, the MOC does not drive the climate change in our simulations.
3) The effective heat capacity governing the rate of surface temperature change depends crucially on the thermohaline stratification of the ocean. A cold sea surface is more susceptible to rapid warming than is a warm sea surface to rapid cooling because warming from above stratifies the water column.
4) The presence of a high-latitude halocline enables rapid changes in sea ice cover that can potentially be completely out of phase with the long-term drift of the climate and deep ocean temperatures.

REFERENCES

Adcroft, A., and J.-M. Campin, 2004: Rescaled height coordinates for accurate representation of free-surface flows in ocean circulation models. *Ocean Modell.,* **7,** 269–284.

Armour, K. C., I. Eisenman, E. Blanchard-Wrigglesworth, K. E. McCusker, and C. M. Bitz, 2011: The reversibility of sea ice loss in a state-of-the-art climate model. *Geophys. Res. Lett.,* **38,** L16705, doi:10.1029/2011GL048739.

Bitz, C., J. Chiang, W. Cheng, and J. Barsugli, 2007: Rates of thermohaline recovery from freshwater pulses in modern, Last Glacial Maximum, and greenhouse warming climates. *Geophys. Res. Lett.,* **34,** L07708, doi:10.1029/2006GL029237.

Braconnot, P., and Coauthors, 2007: Results of PMIP2 coupled simulations of the Mid-Holocene and Last Glacial Maximum—Part 1: Experiments and large-scale features. *Climate Past,* **3,** 261–277.

Broecker, W. S., 1990: Salinity history of the northern Atlantic during the last deglaciation. *Paleoceanography,* **5,** 459–467.

——, D. M. Peteet, and D. Rind, 1985: Does the ocean–atmosphere system have more than one stable mode of operation? *Nature,* **315,** 21–26.

——, G. Bond, M. Klas, G. Bonani, and W. Wolfli, 1990: A salt oscillator in the glacial Atlantic? 1. The concept. *Paleoceanography,* **5,** 469–477.

Budyko, M., 1969: The effect of solar radiation variations on the climate of the earth. *Tellus,* **21,** 611–619.

Campin, J.-M., J. Marshall, and D. Ferreira, 2008: Sea ice–ocean coupling using a rescaled vertical coordinate z^*. *Ocean Modell.,* **24,** 1–14.

Cheng, W., C. M. Bitz, and J. C. Chiang, 2007: Adjustment of the global climate to an abrupt slowdown of the Atlantic meridional overturning circulation. *Ocean Circulation: Mechanisms and Impacts*, Geophys. Monogr., Vol. 173, Amer. Geophys. Union, 295–313.

Clement, A. C., and L. C. Peterson, 2008: Mechanisms of abrupt climate change of the last glacial period. *Rev. Geophys.,* **46,** RG4002, doi:10.1029/2006RG000204.

de Vernal, A., and C. Hillaire-Marcel, 2000: Sea-ice cover, sea-surface salinity and halo-/thermocline structure of the northwest North Atlantic: Modern versus full glacial conditions. *Quat. Sci. Rev.,* **19,** 65–85.

Donohoe, A., and D. S. Battisti, 2011: Atmospheric and surface contributions to planetary albedo. *J. Climate,* **24,** 4402–4418.

Eisenman, I., 2012: Factors controlling the bifurcations structure of sea ice retreat. *J. Geophys. Res.,* **117,** D01111, doi:10.1029/2011JD016164.

Enderton, D., and J. Marshall, 2009: Explorations of atmosphere–ocean–ice climates on an aquaplanet and their meridional energy transports. *J. Atmos. Sci.,* **66,** 1593–1611.

Ferreira, D., J. Marshall, and J.-M. Campin, 2010: Localization of deep water formation: Role of atmospheric moisture transport and geometrical constraints on ocean circulation. *J. Climate,* **23,** 1456–1476.

——, ——, and B. E. J. Rose, 2011: Climate determinism revisited: Multiple equilibria in a complex climate model. *J. Climate,* **24,** 992–1012.

Gent, P., and J. C. McWilliams, 1990: Isopycnal mixing in ocean circulation models. *J. Phys. Oceanogr.,* **20,** 150–155.

Gildor, H., and E. Tziperman, 2003: Sea-ice switches and abrupt climate change. *Philos. Trans. Roy. Soc. London,* **361A,** 1935–1944.

Hawkins, E., R. S. Smith, L. C. Allison, J. M. Gregory, T. J. Woollings, H. Pohlmann, and B. de Cuevas, 2011: Bistability of the Atlantic overturning circulation in a global climate model and links to ocean freshwater transport. *Geophys. Res. Lett.,* **38,** L10605, doi:10.1029/2011GL047208.

Huybers, P., 2011: Combined obliquity and precession pacing of late Pleistocene deglaciations. *Nature,* **480,** 229–232.

——, and C. Wunsch, 2004: A depth-derived Pleistocene age model: Uncertainty estimates, sedimentation variability, and nonlinear climate change. *Paleoceanography,* **19,** PA1028, doi:10.1029/2002PA000857.

Imbrie, J., and Coauthors, 1984: The orbital theory of Pleistocene climate: Support from a revised chronology of the marine $\delta^{18}O$ record. *Milankovitch and Climate, Part 1*, A. Berger et al., Eds., D. Reidel, 269–305.

Jackett, D. R., and T. J. Mcdougall, 1995: Minimal adjustment of hydrographic profiles to achieve static stability. *J. Atmos. Oceanic Technol.,* **12,** 381–389.

Klinger, B. A., and J. Marotzke, 2000: Meridional heat transport by the subtropical cell. *J. Phys. Oceanogr.,* **30,** 696–705.

——, J. Marshall, and U. Send, 1996: Representation of convective plumes by vertical adjustment. *J. Geophys. Res.,* **101** (C8), 18 175–18 182.

Li, C., D. S. Battisti, D. P. Schrag, and E. Tziperman, 2005: Abrupt climate shifts in Greenland due to displacements of the sea ice edge. *Geophys. Res. Lett.,* **32,** L19702, doi:10.1029/2005GL023492.

——, ——, and C. M. Bitz, 2010: Can North Atlantic sea ice anomalies account for Dansgaard–Oeschger climate signals? *J. Climate,* **23,** 5457–5475.

Loutre, M.-F., D. Paillard, F. Vimeux, and E. Cortijo, 2004: Does mean annual insolation have the potential to change the climate? *Earth Planet. Sci. Lett.,* **221,** 1–14.

Loving, J. L., and G. K. Vallis, 2005: Mechanisms for climate variability during glacial and interglacial periods. *Paleoceanography,* **20,** PA4024, doi:10.1029/2004PA001113.

Manabe, S., and R. J. Stouffer, 1995: Simulation of abrupt climate change induced by freshwater input to the North Atlantic Ocean. *Nature,* **378,** 165–167.

Marotzke, J., and M. Botzet, 2007: Present-day and ice-covered equilibrium states in a comprehensive climate model. *Geophys. Res. Lett.,* **34,** L16704, doi:10.1029/2006GL028880.

Marshall, J., A. Adcroft, C. Hill, L. Perelman, and C. Heisey, 1997: A finite-volume, incompressible Navier Stokes model for studies of the ocean on parallel computers. *J. Geophys. Res.,* **102,** 5753–5766.

——, ——, J.-M. Campin, C. Hill, and A. White, 2004: Atmosphere–ocean modeling exploiting fluid isomorphisms. *Mon. Wea. Rev.,* **132,** 2882–2894.

——, D. Ferreira, J.-M. Campin, and D. Enderton, 2007: Mean climate and variability of the atmosphere and ocean on an aquaplanet. *J. Atmos. Sci.,* **64,** 4270–4286.

McManus, J. F., R. François, J.-M. Gherardi, L. D. Keigwin, and S. Brown-Leger, 2004: Collapse and rapid resumption of Atlantic meridional circulation linked to deglacial climate changes. *Nature,* **428,** 834–837.

Molteni, F., 2003: Atmospheric simulations using a GCM with simplified physical parametrizations. I: Model climatology and variability in multi-decadal experiments. *Climate Dyn.,* **20,** 175–191.

North, G. R., 1990: Multiple solutions in energy balance climate models. *Palaeogeogr. Palaeoclimatol. Palaeoecol.,* **82,** 225–235.

——, L. Howard, D. Pollard, and B. Wielicki, 1979: Variational formulation of Budyko–Sellers climate models. *J. Atmos. Sci.,* **36,** 255–259.

Overland, J. E., and P. Turet, 1994: Variability of the atmospheric energy flux across 70°N computed from the GFDL data set. *The Polar Oceans and Their Role in Shaping the Global Environment, Geophys. Monogr.,* Vol. 85, Amer. Geophys. Union, 313–325.

Paillard, D., 1998: The timing of Pleistocene glaciations from a simple multiple-state climate model. *Nature,* **391,** 378–381.

Porter, D. F., J. J. Cassano, M. C. Serreze, and D. N. Kindig, 2010: New estimates of the large-scale Arctic atmospheric energy budget. *J. Geophys. Res.,* **115,** D08108, doi:10.1029/2009JD012653.

Rahmstorf, S., 2002: Ocean circulation and climate during the past 120,000 years. *Nature,* **419,** 207–214.

——, and Coauthors, 2005: Thermohaline circulation hysteresis: A model intercomparison. *Geophys. Res. Lett.,* **32,** L23605, doi:10.1029/2005GL023655.

Redi, M. H., 1982: Oceanic isopycnal mixing by coordinate rotation. *J. Phys. Oceanogr.,* **12,** 1154–1158.

Rind, D., D. Shindell, J. Perlwitz, J. Lerner, P. Lonergan, J. Lean, and C. McLinden, 2004: The relative importance of solar and anthropogenic forcing of climate change between the Maunder Minimum and the present. *J. Climate,* **17,** 906–929.

Roe, G. H., 2006: In defense of Milankovitch. *Geophys. Res. Lett.,* **33,** L24703, doi:10.1029/2006GL027817.

Rose, B. E. J., and J. Marshall, 2009: Ocean heat transport, sea ice, and multiple climate states: Insights from energy balance models. *J. Atmos. Sci.,* **66,** 2828–2843.

——, and D. Ferreira, 2013: Ocean heat transport and water vapor greenhouse in a warm equable climate: A new look at the low gradient paradox. *J. Climate,* **26,** 2117–2136.

Seager, R., and D. S. Battisti, 2007: Challenges to our understanding of the general circulation: Abrupt climate change. *The Global Circulation of the Atmosphere,* T. Schneider and A. H. Sobel, Eds., Princeton University Press, 331–371.

Serreze, M. C., A. P. Barrett, A. G. Slater, M. Steele, J. Zhang, and K. E. Trenberth, 2007: The large-scale energy budget of the Arctic. *J. Geophys. Res.,* **112,** D11122, doi:10.1029/2006JD008230.

Stouffer, R. J., 2004: Time scales of climate response. *J. Climate,* **17,** 209–217.

——, and Coauthors, 2006: Investigating the causes of the response of the thermohaline circulation to past and future climate changes. *J. Climate,* **19,** 1365–1387.

Tziperman, E., M. E. Raymo, P. Huybers, and C. Wunsch, 2006: Consequences of pacing the Pleistocene 100 kyr ice ages by nonlinear phase locking to Milankovitch forcing. *Paleoceanography,* **21,** PA4206, doi:10.1029/2005PA001241.

Wang, Z., and L. A. Mysak, 2006: Glacial abrupt climate changes and Dansgaard–Oeschger oscillations in a coupled climate model. *Paleoceanography,* **21,** PA2001, doi:10.1029/2005PA001238.

Winton, M., 2000: A reformulated three-layer sea ice model. *J. Atmos. Oceanic Technol.,* **17,** 525–531.

——, 2006: Does the arctic sea ice have a tipping point? *Geophys. Res. Lett.,* **33,** L23504, doi:10.1029/2006GL028017.

——, and E. Sarachik, 1993: Thermohaline oscillations induced by strong steady salinity forcing of ocean general circulation models. *J. Phys. Oceanogr.,* **23,** 1389–1410.

Wunsch, C., 2006: Abrupt climate change: An alternative view. *Quat. Res.,* **65,** 191–203.

——, 2010: Towards understanding the Paleocean. *Quat. Sci. Rev.,* **29,** 1960–1967.

Zachos, J., M. Pagani, L. Sloan, E. Thomas, and K. Billups, 2001: Trends, rhythms, and aberrations in global climate 65 Ma to present. *Science,* **292,** 686–693.